
UNIFYING SCALE-AWARE DEPTH PREDICTION AND PERCEPTUAL PRIORS FOR MONOCULAR ENDOSCOPE POSE ESTIMATION AND TISSUE RECONSTRUCTION

Muzammil Khan^{1*}Enzo Kerkhof²Matteo Fusaglia²Koert Kuhlmann²Theo Ruers²Françoise J. Siepel¹

¹The Robotics and Mechatronics Group, University of Twente,
Drienerlolaan 5, 7522 NB Enschede, The Netherlands

²The Department of Surgical Oncology, The Netherlands Cancer Institute-Antoni van Leeuwenhoek,
Plesmanlaan 121, 1066 CX, Amsterdam, The Netherlands

m.khan@utwente.nl, e.kerkhof@nki.nl, m.fusaglia@nki.nl,
k.kuhlmann@nki.nl, t.ruers@nki.nl, f.j.siepel@utwente.nl

August 18, 2025

ABSTRACT

Accurate endoscope pose estimation and 3D tissue surface reconstruction significantly enhances monocular minimally invasive surgical procedures by enabling accurate navigation and improved spatial awareness. However, monocular endoscope pose estimation and tissue reconstruction face persistent challenges, including depth ambiguity, physiological tissue deformation, inconsistent endoscope motion, limited texture fidelity, and a restricted field of view. To overcome these limitations, a unified framework for monocular endoscopic tissue reconstruction that integrates scale-aware depth prediction with temporally-constrained perceptual refinement is presented. This framework incorporates a novel MAPIS-Depth module, which leverages Depth Pro for robust initialisation and Depth Anything for efficient per-frame depth prediction, in conjunction with L-BFGS-B optimisation, to generate pseudo-metric depth estimates. These estimates are temporally refined by computing pixel correspondences using RAFT and adaptively blending flow-warped frames based on LPIPS perceptual similarity, thereby reducing artefacts arising from physiological tissue deformation and motion. To ensure accurate registration of the synthesised pseudo-RGBD frames from MAPIS-Depth, a novel WEMA-RTDL module is integrated, optimising both rotation and translation. Finally, truncated signed distance function-based volumetric fusion and marching cubes are applied to extract a comprehensive 3D surface mesh. Evaluations on HEVD and SCARED, with ablation and comparative analyses, demonstrate the framework's robustness and superiority over state-of-the-art methods.

Keywords Monocular reconstruction · Depth estimation · Endoscope pose estimation · Foundation model · Monocular endoscopy.

1 Introduction

Minimally invasive surgery (MIS), including monocular and stereoscopic endoscopy as well as robotic systems, has transformed modern surgical practice by reducing incision size, limiting tissue trauma and lowering postoperative morbidity and recovery times [1, 2]. Among these approaches, monocular minimally invasive surgery (MMIS) remains

*Preprint Notice - This work has been submitted to *IEEE Access* for possible publication. This is the author's original manuscript and has not undergone peer review. Subsequent versions of this manuscript may differ from this one. The final published version, if accepted, will be available via IEEE Xplore. Corresponding author: m.khan@utwente.nl

the most widely adopted technique due to its lower cost, simpler setup, and broad accessibility across diverse clinical settings [3, 4]. However, MMIS is inherently constrained by a limited field of view and the absence of direct depth cues, forcing surgeons to rely on indirect visual indicators such as shading, motion, or anatomical landmarks to interpret spatial relationships. These perceptual limitations are further exacerbated in anatomically complex regions such as those involving hidden tumours, overlapping tissues, or proximity to critical vessels, posing challenges to accurate navigation and intraoperative decision-making. Whilst stereoscopic and robotic systems partially alleviate these issues through binocular disparity or enhanced visual interfaces, their adoption remains limited due to higher costs and integration complexities. In this context, recent advances in computer vision and deep learning have enabled computational techniques that can infer depth and spatial structure directly from monocular endoscopic images [5, 6, 7, 8]. These approaches offer a hardware-agnostic solution to enhance spatial awareness and intraoperative guidance within existing MMIS workflows, representing a significant step towards safer, more precise, and context-aware MIS procedures.

Despite these advancements, achieving accurate 3D surface reconstruction in MMIS remains technically challenging, primarily due to the lack of metric depth cues, which are essential for precise spatial measurements and accuracy in navigation [9, 10]. Monocular systems lack stereoscopic disparity, relying instead on secondary visual cues such as motion parallax, shading gradients, and occlusion boundaries [11, 12, 13, 14]. However, these inferred depth cues often result in non-metric or relative depth estimates, which are prone to noise and heavily dependent on the structural properties of the scene. Furthermore, the MMIS environment introduces dynamic, non-rigid deformations due to physiological processes such as respiration, complicating robust depth estimation and temporal alignment. These challenges significantly hinder the ability to achieve consistent metric depth accuracy [5, 6, 7].

Another major challenge in 3D reconstruction is the reliable registration of RGB-D frames, particularly in low-texture, homogeneous tissue regions commonly encountered in MMIS. The scarcity of distinctive features in these regions impairs the identification of stable spatial reference points, which are critical for effective feature matching and alignment [8, 15]. This issue is further exacerbated in complex anatomical environments, where the endoscope must navigate through narrow, curved, and multi-layered pathways. These constraints necessitate high-precision depth and endoscope pose estimation strategies to ensure accurate and stable reconstructions [16, 17].

1.1 Contribution

The primary contributions of this research are encapsulated in the design and development of a unified framework for monocular endoscope pose estimation and tissue reconstruction, which integrates scale-aware depth prediction with perceptually guided refinement and leverages both data-driven and optimisation-based methodologies. It comprises the following three core modules:

- **Metric-Aware Perceptual Image Similarity Depth (MAPIS-Depth) module:** A novel depth estimation module that combines the strengths of the foundation models Depth Pro [18] and Depth Anything [19], the former used for robust initialisation and the latter for efficient per-frame inference. The resulting depth maps are further refined using L-BFGS-B optimisation. To enhance temporal consistency and suppress artefacts from tissue deformation and motion, RAFT-based optical flow [20] is used to establish inter-frame correspondences, and LPIPS (Learned Perceptual Image Patch Similarity) [21] is employed to guide adaptive perceptual blending.
- **Weighted Exponential Moving Average-based Rotation-Translation Dog-Leg (WEMA-RTDL) module:** A robust, multiscale $\mathcal{SO}(3)$ – $\mathcal{SE}(3)$ decoupled dog-leg optimisation strategy [22], developed to improve frame-to-frame endoscope pose estimation in low-texture, homogeneous regions. It incorporates a WEMA refinement mechanism [22, 23] to ensure stable and accurate transformation estimates.
- **Volumetric fusion module:** A truncated signed distance function (TSDF)-based [24] approach for smooth monocular tissue surface reconstruction, with Marching Cubes [25] used to extract a triangulated mesh [26].

Furthermore, the proposed framework is validated across multiple benchmark datasets, including Hamlyn Endoscopic Video Dataset (HEVD) [26] and Stereo Correspondence and Reconstruction of Endoscopic Data (SCARED) [16], with comprehensive performance assessments conducted through ablation and comparative studies.

2 Related Works

Recent years have witnessed significant progress in monocular surface reconstruction, driven by advances in both learning-based and optimisation-based methodologies [27, 28, 29, 30, 31]. These approaches can be broadly categorised into offline and online methods, with online reconstruction being essential for real-time applications such as MMIS procedures. Online techniques typically involve real-time depth estimation, spatial correspondence modelling, and

surface integration to produce temporally consistent monocular reconstructions [32, 33]. These techniques are further categorised into geometry-driven, end-to-end deep learning-based, and hybrid approaches, each offering distinct advantages in balancing computational efficiency, accuracy, and adaptability to complex environments [34, 35, 36, 37, 38].

2.1 Geometry-driven techniques

Classical methods for monocular reconstruction commonly rely on geometric techniques involving feature detection, matching, and camera motion estimation [39, 40]. Algorithms such as ORB-SLAM [41], ORB-SLAM3 [42], and PTAM [43] employ local descriptors including SIFT, SURF, and ORB [44, 45, 46], combined with pose optimisation via Perspective-n-Point solvers and bundle adjustment [47, 48]. Probabilistic formulations such as [49, 50, 51] have improved robustness to motion uncertainty, however, these approaches often produce sparse reconstructions and underperform in texture-sparse or low-contrast environments typical in MMIS. Variational methods have improved map density [52, 53, 54, 55, 56], yet generally lack depth scale estimation and assume rigid scene structure, limitations that are particularly pronounced in anatomically dynamic surgical settings.

2.2 End-to-end deep learning-based techniques

Deep learning-based techniques have transformed monocular reconstruction by unifying depth prediction, feature extraction, and motion estimation within a single trainable framework [57, 58]. Unlike traditional methods that depend on hand-crafted features, these approaches leverage convolutional and recurrent neural networks to infer depth and pose directly from image sequences [59, 60]. PoseNet [61] and DeepVO [62] exemplify architectures that regress camera motion, while models such as SfMLearner [58] and UnDeepVO [63] jointly estimate depth and ego-motion, often with self-supervised loss formulations. Other works like NICESLAM [64] utilise hierarchical neural fields for dense reconstruction, and Monodepth [65] demonstrates how dense disparity can be recovered from monocular inputs. However, the effectiveness of these methods in MMIS contexts is often constrained by their reliance on large-scale labelled datasets, which are difficult to obtain in medical domains [66]. This underscores the need for data-efficient solutions that can generalise across anatomical variations.

2.3 Hybrid techniques

To overcome the limitations of purely geometric or learning-based methods, recent research has explored hybrid frameworks that combine learning-driven depth inference with geometric refinement and surface integration. For example, Endo-Depth-and-Motion [26] integrates Monodepth2-based depth prediction with photometric consistency for motion estimation, followed by volumetric fusion via TSDF [24]. Similarly, EndoGSLAM [67] applies 3D Gaussian splatting and differentiable rasterisation [68] to reconstruct detailed anatomical surfaces in real time. It includes both high-fidelity and fast variants, with pre-filtering mechanisms to exclude unreliable pixel regions and improve temporal coherence. Other modular designs such as BodySLAM [69] incorporate deep depth networks like ZoeDepth [70] for monocular depth estimation and CyclePose for pose estimation, fusing these with traditional techniques such as pose graph optimisation and ICP [71].

Overall, these works highlight the growing trend towards integrating perceptual depth cues, data-driven learning, and geometric consistency for robust and scalable monocular reconstruction, especially under the constraints of tissue deformation, low texture, and scale ambiguity found in MMIS environments.

3 Methodology

The proposed framework integrates three core modules: MAPIS-Depth, which generates scale-consistent depth estimates; WEMA-RTDL, a robust pose estimation module for registering pseudo-RGBD frames; and a volumetric fusion module, which enables high-resolution tissue surface reconstruction.

3.1 MAPIS-Depth Module

The MAPIS-Depth module, illustrated in Fig. 1, plays a central role in the proposed framework by producing high-fidelity scale-consistent depth maps essential for accurate tissue reconstruction. It leverages two vision transformer-based foundation models, Depth Pro [18] and Depth Anything [19], to capture complex spatial hierarchies and structural variations typical of MMIS environments [72]. Depth Pro facilitates zero-shot metric depth prediction with precise boundary delineation through multi-scale attention, while Depth Anything provides rapid per-frame inference and improved robustness to specular highlights and visual distortions, both of which are prevalent in endoscopic imaging.

To optimise inference speed while maintaining scale consistency, Depth Pro is employed solely for the initialisation stage, wherein it estimates both the depth and the corresponding focal length for the first frame in the input sequence. For subsequent frames, depth is inferred using the more computationally efficient Depth Anything model. Specifically, the first frame, \mathcal{J}_1 , is processed by Depth Pro to estimate its corresponding pseudo-metric depth estimate (MDE) \mathcal{D}_1^{mde} and a focal length f_{pred} . Simultaneously, the same frame is input into Depth Anything, which predicts the associated disparity map d_1^{mde} . To enable scale-aware depth estimation for the remaining frames, a pseudo-stereo baseline \mathcal{B} is estimated from the initial frame by utilising \mathcal{D}_1^{mde} , d_1^{mde} , and f_{pred} . This baseline represents the effective distance between two virtual camera centres and emulates a stereo configuration within a monocular context. The optimal value of \mathcal{B} is computed by minimising the discrepancy between the known depth \mathcal{D}_1^{mde} and the depth derived from the disparity map, as follows:

$$\mathcal{B} = \arg \min_{\hat{\mathcal{B}}} (\mathcal{D}_1^{mde} - \mathcal{D}_1^{est})^2 \quad (1)$$

where $\mathcal{D}_1^{est} = \frac{f_{pred} \cdot \hat{\mathcal{B}}}{d_1^{mde}}$ represents the computed depth, and $\hat{\mathcal{B}}$ denotes the initial estimate of the baseline. The objective function is minimised using the L-BFGS-B algorithm [73], which iteratively refines $\hat{\mathcal{B}}$ to yield the optimal baseline \mathcal{B} . Once \mathcal{B} is determined, the subsequent frames are directly processed by the Depth Anything model to predict their respective disparity maps $\{d_i^{mde}\}_{i=2}^N$, where N denotes the total number of frames. The corresponding MDEs $\{\mathcal{D}_i^{mde}\}_{i=2}^N$ are then computed using the relation $\mathcal{D}_i^{mde} = \frac{f_{pred} \cdot \mathcal{B}}{d_i^{mde}}$.

Up to this point, the process treats each consecutive image pair, \mathcal{J}_{i-1} and \mathcal{J}_i , as independent snapshots. However, this approach overlooks the temporal dynamics inherent in MMIS sequences, including physiological tissue deformations and endoscope movement. To compensate for this, the sequence $\{\mathcal{D}_i^{mde}\}_{i=1}^N$, containing N MDEs corresponding to the input image sequence $\{\mathcal{J}_i\}_{i=1}^N$, is refined using optical flow analysis and LPIPS maps. For each pair of consecutive frames $\{\mathcal{J}_{i-1}, \mathcal{J}_i\}$, dense optical flow is computed to estimate pixel-wise displacements, which map positions from \mathcal{J}_{i-1} to their correspondences in \mathcal{J}_i . This analysis is performed using the Recurrent All-Pairs Field Transforms (RAFT) method [20], which yields high-resolution flow fields with precise pixel-level accuracy. Its use of multi-scale correlation volumes enables robust flow estimation, which is critical for achieving consistent temporal alignment of depth predictions.

Once the optical flow $(\mathcal{U}, \mathcal{V})$ is computed, it is used to warp \mathcal{D}_{i-1}^{mde} using the *remap* function in *OpenCV* [74], producing a warped depth map, \mathcal{D}_i^{warp} . Furthermore, to preserve the structural integrity of the depth map and ensure that key features are not lost during the warping process, a bilateral filtering [75] step is applied to \mathcal{D}_i^{warp} as follows:

$$\begin{aligned} \mathcal{D}_i^{warp'}(\mathbf{x}) = & \frac{1}{W(\mathbf{x})} \sum_{\mathbf{y} \in \Omega} \mathcal{D}_i^{warp}(\mathbf{y}) \cdot \exp\left(-\frac{\|\mathbf{x} - \mathbf{y}\|^2}{2\sigma_d^2}\right) \\ & \cdot \exp\left(-\frac{|\mathcal{D}_i^{warp}(\mathbf{x}) - \mathcal{D}_i^{warp}(\mathbf{y})|^2}{2\sigma_r^2}\right) \end{aligned} \quad (2)$$

where $\mathcal{D}_i^{warp'}$ is the filtered warped depth map, $W(\mathbf{x})$ is the normalisation term, Ω is the neighbourhood of \mathbf{x} , with \mathbf{x} and \mathbf{y} being the pixel indices in Ω . The parameters σ_d and σ_r control the spatial extent and the range of intensity considered for smoothing, respectively.

Additionally, the image pair $\{\mathcal{J}_{i-1}, \mathcal{J}_i\}$ from the sequence $\{\mathcal{J}_i\}_{i=1}^N$ is input into a pre-trained AlexNet model [76], which has been trained on the ImageNet dataset with its classification head removed. This model generates a sequence of feature maps $\{\Phi_l(\mathcal{J}_i)\}_{i=1}^N$, corresponding to the l^{th} layer of the AlexNet architecture. These feature maps are then used to compute the LPIPS score \mathcal{S}_{lips} [21], for each pair $\{\mathcal{J}_{i-1}, \mathcal{J}_i\}$, which assesses their perceptual similarity:

$$\mathcal{S}_{lips} = \sum_l \lambda_l \left[\sum_l \|\hat{\Phi}_l^c(\mathcal{J}_i) - \hat{\Phi}_l^c(\mathcal{J}_{i-1})\|_2^2 \right] \quad (3)$$

Here, $\hat{\Phi}_l^c(\mathcal{J}_i)$ denotes the c^{th} channel of the normalised feature map $\hat{\Phi}_l(\mathcal{J}_i) = \frac{\Phi_l(\mathcal{J}_i)}{\|\Phi_l(\mathcal{J}_i)\|_2}$. A lower \mathcal{S}_{lips} score indicates greater perceptual similarity between \mathcal{J}_{i-1} and \mathcal{J}_i , and thus higher confidence in the warped depth map $\mathcal{D}_i^{warp'}$. Conversely, a higher LPIPS score suggests reduced perceptual similarity, leading to increased reliance on the original depth estimate \mathcal{D}_i^{mde} . The final MAPIS-Depth maps are then computed through a weighted linear blending of $\mathcal{D}_i^{warp'}$ and \mathcal{D}_i^{mde} as follows:

$$\hat{\mathcal{D}}_i = \mathcal{S}_{lips} \cdot \mathcal{D}_i^{warp'} + (1 - \mathcal{S}_{lips}) \cdot \mathcal{D}_i^{mde} \quad (4)$$

Here, $\hat{\mathcal{D}}_i$ denotes the refined MAPIS-Depth map corresponding to the i^{th} image in the sequence. The impact of this acceleration on performance and accuracy is further analysed in Section 4.3.

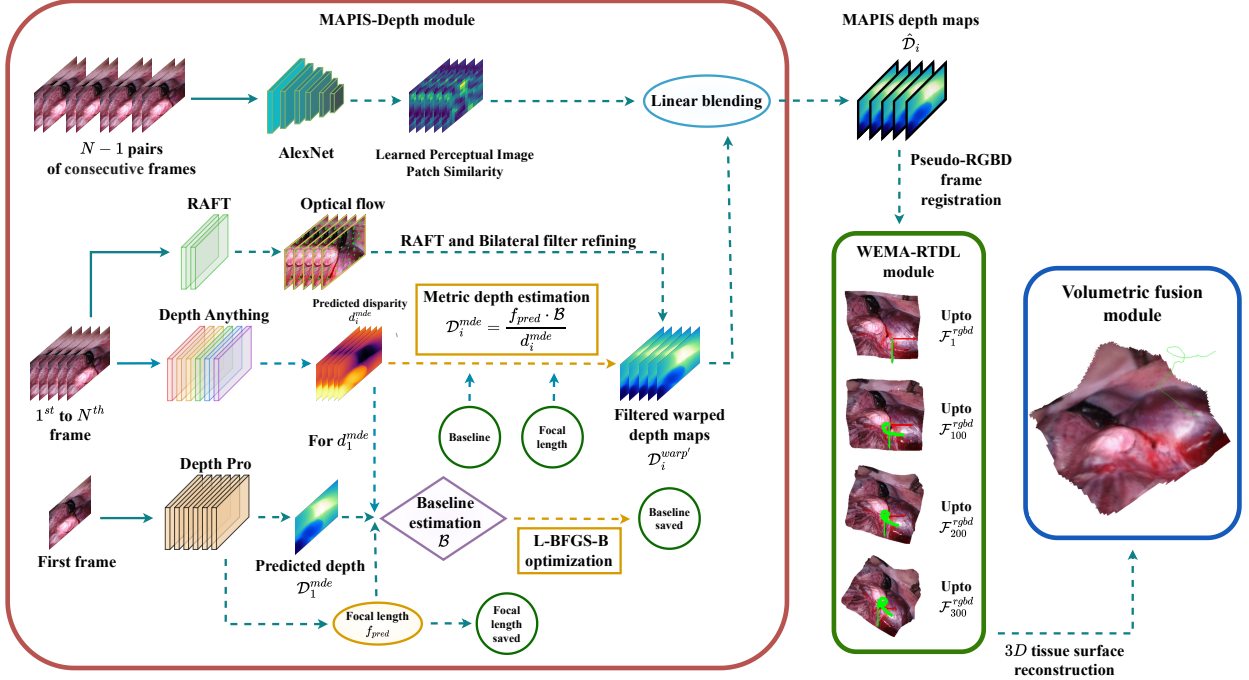


Figure 1: Methodology of the proposed framework with three modules: MAPIS-Depth, WEMA-RTDL, and Volumetric Fusion.

3.2 WEMA-RTDL module

The refined MAPIS-Depth maps \hat{D}_i are combined with their corresponding RGB images \mathcal{I}_i to form pseudo-RGBD frames, denoted as \mathcal{F}_i^{rgbd} . From the set $\{\mathcal{F}_i^{rgbd}\}_{i=1}^N$, each frame \mathcal{F}_j^{rgbd} , starting from \mathcal{F}_0^{rgbd} , is selected as a keyframe K_j^{ref} , where $j = \alpha \cdot m$, with $\alpha = 2$ as a fixed non-negative integer and $m \in [0, \lfloor N/2 \rfloor] \cap \mathbb{Z}$. Each intermediate frame to be aligned with a reference keyframe is denoted as $K_{j,r}^{track}$, while the subsequent keyframe K_{j+1}^{ref} is aligned with respect to the preceding one, K_j^{ref} .

To enable robust frame alignment under varying motion conditions, multi-scale image pyramids are constructed for each frame pair. Specifically, pyramids $\{K_{j,r}^{track,\Lambda}\}_{\Lambda=1}^{\Lambda_{pyr}}$ and $\{K_j^{ref,\Lambda}\}_{\Lambda=1}^{\Lambda_{pyr}}$ are generated for $K_{j,r}^{track}$ and K_j^{ref} , respectively. Here, $\Lambda_{pyr} = 5$ denotes the total number of pyramid levels, with each level downsampled by a factor of $d = 0.5$. These pyramids facilitate multi-resolution analysis, allowing the alignment to begin at a coarse spatial scale—useful for handling large inter-frame displacements and progressively refining the transformation at higher resolutions. This hierarchical strategy ensures robust and precise alignment of pseudo-RGBD frames.

3.2.1 Rotation-Translation Decoupling

The estimation of endoscope motion begins by initialising the rotation parameters $\mathbf{x}_{j,r}^{so3} \in \mathcal{SO}(3)$ and the combined rotation-translation parameters $\mathbf{x}_{j,r}^{se3} \in \mathcal{SE}(3)$ as identity matrices for the first pyramid level ($\Lambda = 1$) corresponding to $K_{j,r}^{track,\Lambda}$. The photometric error is computed as follows [77]:

$$e_{j,r}^k = \|\mathcal{I}_j(\mathbf{p}) - \mathcal{I}_{j,r}(\mathbf{p}')\|_2 \quad (5)$$

where $e_{j,r}^k$ denotes the photometric error at the k^{th} optimisation iteration. The term $\mathcal{I}_j(\mathbf{p})$ represents the intensity at pixel \mathbf{p} in the reference image $K_j^{ref,\Lambda}$, and $\mathcal{I}_{j,r}(\mathbf{p}')$ denotes the interpolated intensity at the transformed location \mathbf{p}' in the tracked frame $K_{j,r}^{track,\Lambda}$. The transformed position \mathbf{p}' is obtained via:

$$\mathbf{p}' = \mathcal{C}_j \mathcal{T}_j^{-1} \mathcal{T}_{j,r} \mathcal{C}_{j,r}^{-1} \mathcal{D}_{j,r} \mathbf{p}$$

where \mathcal{C}_j and $\mathcal{C}_{j,r}$ are the intrinsic matrices corresponding to the reference and tracked frames, respectively, and \mathcal{T}_j and $\mathcal{T}_{j,r}$ are the transformation matrices derived from \mathbf{x}_j^{se3} and $\mathbf{x}_{j,r}^{se3}$. The matrix $\mathbf{x}_{j,r}^{se3}$ is constructed as:

$$\mathbf{x}_{j,r}^{se3} = \begin{bmatrix} \mathbf{x}_{j,r}^{so3} \odot \mathbf{x}_{j,rot}^{se3} & \mathbf{x}_{j,r}^{so3} \odot \mathbf{x}_{j,trans}^{se3} \\ \mathbf{0} & 1 \end{bmatrix} \quad (6)$$

Here, $\mathbf{x}_{j,rot}^{se3}$ and $\mathbf{x}_{j,trans}^{se3}$ represent the 3×3 rotation and 3×1 translation components, respectively, and \odot denotes standard matrix multiplication.

3.2.2 Optimisation

To optimise the rotation parameters $\mathbf{x}_{j,r}^{so3}$, a dog-leg optimisation scheme is adopted [22], initialised with a trust region radius $\rho \in \mathbb{R}^+$. This radius governs the step size during each iteration by balancing between the steepest descent and Gauss–Newton directions, thereby facilitating efficient convergence [78, 79]:

$$\rho_{gn} = - \left(\mathbf{J}^T \mathbf{J} \right)^{-1} \mathbf{J}^T e_{j,r}^k \quad (7)$$

$$\rho_{sd} = - \mathbf{J}^T e_{j,r}^k \quad (8)$$

Here, ρ_{gn} and ρ_{sd} denote the candidate step sizes $\Delta \mathbf{x}$ derived from the Gauss–Newton and steepest descent strategies, respectively, and \mathbf{J} is the Jacobian matrix of partial derivatives of $e_{j,r}^k$ with respect to $\mathbf{x}_{j,r}^{se3}$. The final update step $\Delta \mathbf{x}$ is selected according to the following rule [22]:

$$\Delta \mathbf{x} = \begin{cases} \rho_{gn} & \text{if } \|\rho_{gn}\| \leq \rho \\ \rho \frac{\rho_{sd}}{\|\rho_{sd}\|} & \text{if } \|\rho_{gn}\| > \rho \text{ and } \|\rho_{sd}\| > \rho \\ (1-s)\rho_{sd} + s\rho_{gn} & \text{if } \|\rho_{gn}\| > \rho \text{ and } \|\rho_{sd}\| < \rho \end{cases} \quad (9)$$

where $h = \frac{\|\rho_{sd}\|^2}{\|\mathbf{J}\rho_{sd}\|^2}$ and s is selected such that $\|\rho_{gn}\| = \|\rho_{sd}\| = \rho$. The trust region radius is adaptively adjusted, effectively navigating the optimisation process and providing an estimate for rotation parameters as follows:

$${}_{est}\mathbf{x}_{j,r}^{so3} = \mathbf{x}_{j,r}^{so3} + \Delta \mathbf{x}_{rot} \quad (10)$$

where $\Delta \mathbf{x}_{rot}$ denotes the rotational component of the step $\Delta \mathbf{x}$.

Following rotation optimisation at the coarsest pyramid level ($\Lambda = 1$), the full transformation parameters $\mathbf{x}_{se3} \in \mathcal{SE}(3)$, encompassing both rotation and translation, are optimised for levels $\Lambda \geq 2$. For $\Lambda = 2$, the previously estimated rotation ${}_{est}\mathbf{x}_{j,r}^{so3}$ is used to initialise the rotational component of \mathbf{x}_{se3} , yielding an initial estimate denoted as ${}_{in}\mathbf{x}_{j,r}^{se3}$. This initial transformation is then refined using the same optimisation procedure described for ${}_{est}\mathbf{x}_{j,r}^{so3}$, with the exception of the update rule in Equation (6). Since both rotation and translation are now subject to refinement, the update follows:

$$\mathbf{x}_{j,r}^{se3} = {}_{in}\mathbf{x}_{j,r}^{se3} \cdot \mathbf{x}_j^{se3} \quad (11)$$

where \cdot denotes standard matrix multiplication. After performing dog-leg optimisation, the refined pose is computed as:

$${}_{est}\mathbf{x}_{j,r}^{se3} \leftarrow \mathbf{x}_{j,r}^{se3} + \Delta \mathbf{x} \quad (12)$$

This iterative process provides robust endoscope pose estimation in terms of \mathbf{x}_{se3} and ensures accurate registration of \mathcal{F}_i^{rgbd} . The estimated $\mathcal{SE}(3)$ pose \mathbf{x}_{se3} is then used to update the camera pose for the tracked frame $K_{j,r}^{track}$.

3.2.3 Regularisation

To stabilise pose estimates and minimise jitter in \mathcal{F}_i^{rgbd} registration, the Exponential Moving Average (EMA) technique is applied to the estimated poses. Given the current estimated pose \mathbf{x}_{se3}^i and the two previous poses \mathbf{x}_{se3}^{i-1} and \mathbf{x}_{se3}^{i-2} , the regularised pose $\mathbf{x}_{se3}^{i,reg}$ is computed as:

$$\mathbf{x}_{se3}^{i,reg} = (\alpha \mathbf{x}_{se3}^i + \beta \mathbf{x}_{se3}^{i-1} + \gamma \mathbf{x}_{se3}^{i-2})s + \mathbf{x}_{se3}^i(1-s) \quad (13)$$

Here, α , β , and γ are weighting factors satisfying $\alpha + \beta + \gamma = 1$, and $s = 1 - \exp(-i * \omega)$ adjusts for the accumulated frame count i using the scaling factor $\omega \in \mathbb{R}^+$. The coefficient s ensures that the regularisation becomes more effective as the frame number becomes larger, since at large frame numbers drift becomes more influencing and hence regularisation stabilises the endoscope poses. This approach ensures smoother camera pose transitions by incorporating historical pose data, effectively reducing noise and enhancing registration robustness in the MMIS environment.

3.3 3D Reconstruction

This module integrates the registered pseudo-RGBD frames using a TSDF approach [26], which efficiently fuses per-frame depth and pose information into a coherent 3D surface representation. Depth measurements are accumulated within a voxel grid as signed distances relative to the nearest observed surface, and are iteratively refined to suppress noise and artefacts [80]. Finally, the Marching Cubes algorithm [25] is applied to extract a smooth and topologically consistent mesh, thereby enhancing monocular imagery with geometrically accurate tissue surface reconstructions.

4 Experimental Results and Discussion

4.1 Dataset

The proposed framework is rigorously evaluated on two benchmark datasets: HEVD [26] and SCARED [16]. The HEVD dataset consists of monocular endoscopic video sequences that are representative of clinical scenarios, including motion blur, specular highlights, physiological tissue deformation, and smoke occlusion, thereby serving as a representative testbed for reconstruction under surgically realistic conditions. In contrast, the SCARED dataset provides precisely calibrated ground truth information derived from structured light projection on porcine anatomy. Its millimetre-scale accuracy and controlled setup enable quantitative assessment in the presence of anatomical complexity and occlusions.

4.2 Evaluation Metrics

To assess the performance of the proposed framework, the consistency in depth estimation, accuracy of endoscope’s estimated pose, and scale-awareness are evaluated.

Depth consistency is evaluated through an ORB-based point-to-point correspondence analysis across temporally adjacent frames [46]. For each pair of consecutive point clouds reconstructed from predicted depth maps, matched 3D points are sampled and the displacement between them are computed. Bar plots of these displacements, along with mean and median statistics, provide a quantitative indicator of temporal smoothness and structural coherence in the estimated depth. Reduced peak displacements signal higher geometric consistency across frames.

Pose estimation results are grouped into four categories: (i) per-axis errors, comprising mean translation (T_{avg}) and mean rotation error (R_{avg}), which quantify axis-wise pose drift across the trajectory; (ii) global errors, which include root mean square error (RMSE), terminal translation error (T_{fin}), and terminal rotation error (R_{fin}), reflecting the accumulated deviation at the end of the sequence; (iii) frame-level errors, measured via relative pose error (RPE), as well as maximum translation (T_{max}) and rotation errors (R_{max}), to capture transient spikes and inter-frame drift; and (iv) statistical proportions, reporting the percentage of poses with error below the mean ($T < T_{\text{avg}}$ and $R < R_{\text{avg}}$), which provide a measure of tracking robustness by indicating the frequency of low-error pose estimates along the trajectory [81, 82].

Scale awareness is assessed using the Trajectory Length Ratio (TLR), defined as the ratio between the estimated trajectory length and the ground truth trajectory length. A TLR close to 1 indicates consistent scaling in estimated poses, while significant deviations from unity indicate scale drift. This metric thus serves as a proxy for global scale fidelity, particularly important in monocular settings where scale ambiguity is a critical challenge.

4.3 Results and Discussion

All experiments are conducted on an NVIDIA GeForce RTX 4080 GPU [83], leveraging its high computational throughput for efficient execution of the framework. The experimental protocol is structured to comprehensively evaluate the proposed framework across diverse MMIS scenarios, including challenging intraoperative conditions such as illumination variation, occlusion, deformation, and smoke. The results encompass both qualitative visualisations and quantitative metrics, spanning depth consistency, pose regularity, and scale fidelity.

The first experiment, illustrated in Fig. 2, evaluates the temporal consistency of depth estimation by the proposed MAPIS-Depth module on an HEVD dataset [26]. Each row in the upper panel of Fig. 2 presents a pair of temporally adjacent frames, \mathcal{I}_{i-1} and \mathcal{I}_i , along with their corresponding depth maps. The top row visualises the depth predictions $\hat{\mathcal{D}}_{i-1}$ and $\hat{\mathcal{D}}_i$ from MAPIS-Depth, while the bottom row shows depth maps $\mathcal{D}_{i-1}^{\text{mde}}$ and $\mathcal{D}_i^{\text{mde}}$ [18]. The final column in both rows presents the absolute difference maps: $|\hat{\mathcal{D}}_i - \hat{\mathcal{D}}_{i-1}|$ and $|\mathcal{D}_i^{\text{mde}} - \mathcal{D}_{i-1}^{\text{mde}}|$, respectively. It is evident that the MAPIS-Depth predictions yield significantly lower inter-frame residuals, indicating smoother and temporally coherent depth transitions. In contrast, the MDE predictions show elevated residuals and inconsistent geometric profiles across adjacent frames, highlighting the lack of temporal regularity.

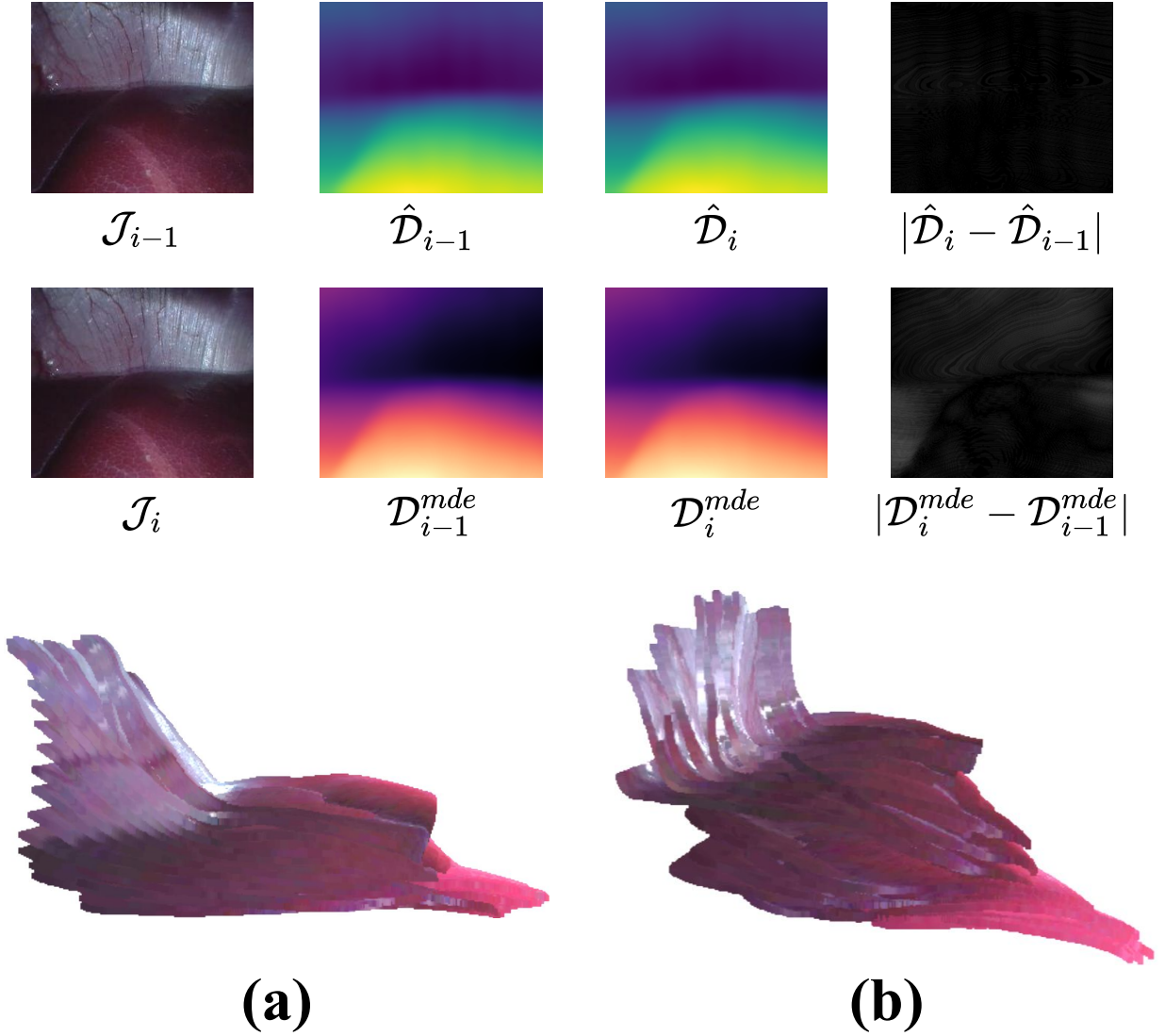


Figure 2: Temporal consistency assessment with MAPIS-Depth and MDE [18]. Top: consecutive frames \mathcal{J}_{i-1} and \mathcal{J}_i with their respective depth predictions and absolute difference maps. Bottom: registered pseudo-RGBD reconstructions show improved geometric continuity using MAPIS-Depth (a) compared to MDE (b). Visualised on the HEVD dataset [26].

Further evidence is provided by the registered point clouds (RPCs) shown at the bottom of Fig. 2. Subfigure (a), generated from MAPIS-Depth maps, demonstrates structurally coherent and artefact-free registration with smooth surface continuity across frames. In contrast, subfigure (b), based on MDE maps, exhibits prominent discontinuities and misalignments, particularly at tissue folds and borders. The complete reconstructions corresponding to Fig. 2 (a) and 2 (b) are demonstrated in Fig. 3 (a) and 3 (b), respectively. These observations confirm that the temporal regularisation introduced by MAPIS-Depth contributes to more consistent depth estimates across time, which is vital for monocular 3D reconstruction in dynamic and low-texture surgical scenes.

The second experiment extends the temporal consistency evaluation of the proposed MAPIS-Depth module across diverse HEVD and SCARED datasets [26, 16], as illustrated in Fig. 4. These datasets encompass varying surgical environments with differences in tissue structure, illumination, and camera motion patterns. Each row in Fig. 4 represents one surgical scene. The first column shows representative RGB frames, followed by MAPIS-Depth predictions for two consecutive frames in the second and third columns. The fourth column presents the absolute

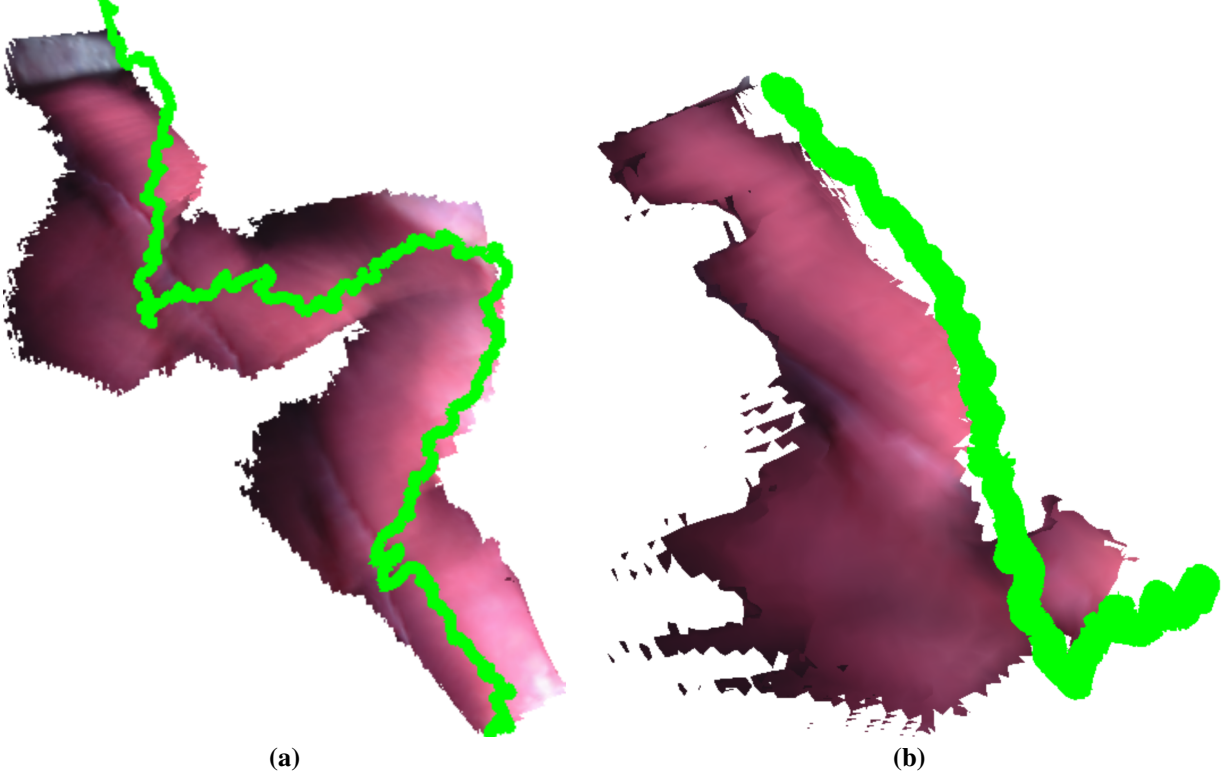


Figure 3: Reconstructed surfaces with estimated camera trajectories (green) on an HEVD dataset [26]: (a) MAPIS-Depth shows smoother paths and denser surfaces; (b) MDE [18] exhibits fragmentation and drift.

difference between these MAPIS-Depth predictions, highlighting minimal inter-frame residuals and confirming strong temporal coherence. In contrast, the fifth and sixth columns show the corresponding MDEs [18], with their respective pixel-wise difference maps shown in the seventh column. These exhibit substantially higher residuals and geometric instability across frames.

To quantitatively evaluate the spatial coherence of consecutive RPCs, Fig. 5 presents a point-to-point correspondence analysis between two temporally adjacent point clouds across the datasets shown in Fig. 4 (a)-(d). For each dataset, ORB features [46] were extracted from successive RGB frames and projected into 3D space using the estimated camera poses and intrinsic parameters. These projections were then sampled and paired across frames to compute displacement magnitudes. Each column in Fig. 5 corresponds to a dataset visualised in Fig. 4. The first and second rows present bar graphs illustrating the displacement magnitudes of the matched point pairs derived from MAPIS-Depth and MDEs [18], respectively. The reduced mean and median values in these graphs clearly demonstrate the superior temporal consistency achieved by MAPIS-Depth. The third and fourth rows display the corresponding 3D scatter plots of the matched point pairs for MAPIS-Depth and MDEs, respectively, providing visual evidence of the alignment quality. As observed, MAPIS-Depth yields lower displacement magnitudes and more tightly clustered spatial alignments, reflecting improved inter-frame consistency and robustness to deformation and motion. In contrast, MDE-based predictions result in larger correspondence errors and scattered point alignments, indicating temporal instability under the dynamic conditions of MIS procedures. These findings quantitatively reinforce the capability of MAPIS-Depth to maintain both temporal coherence across frames, which is an essential requirement for generating reliable 3D tissue reconstructions in surgical environments.

The third experiment evaluates the endoscope pose estimation performance of the proposed framework through comparative benchmarking against four state-of-the-art (SOTA) methods: Endo-2DTAM [84], OneSLAM [85], BodySLAM [86], and Endo-Depth-and-Motion [26]. The evaluation is performed across representative sequences from the SCARED dataset [16], with results summarised in Table 1. The proposed method consistently outperforms existing approaches in both per-axis and global pose error metrics, including average translation (T_{avg}), average rotation (R_{avg}), and root mean square error. Notably, it also yields lower terminal errors (T_{fin} , R_{fin}) and reduced frame-level drift, as reflected by metrics such as RPE, T_{max} , and R_{max} . These improvements demonstrate the robustness and precision of the proposed

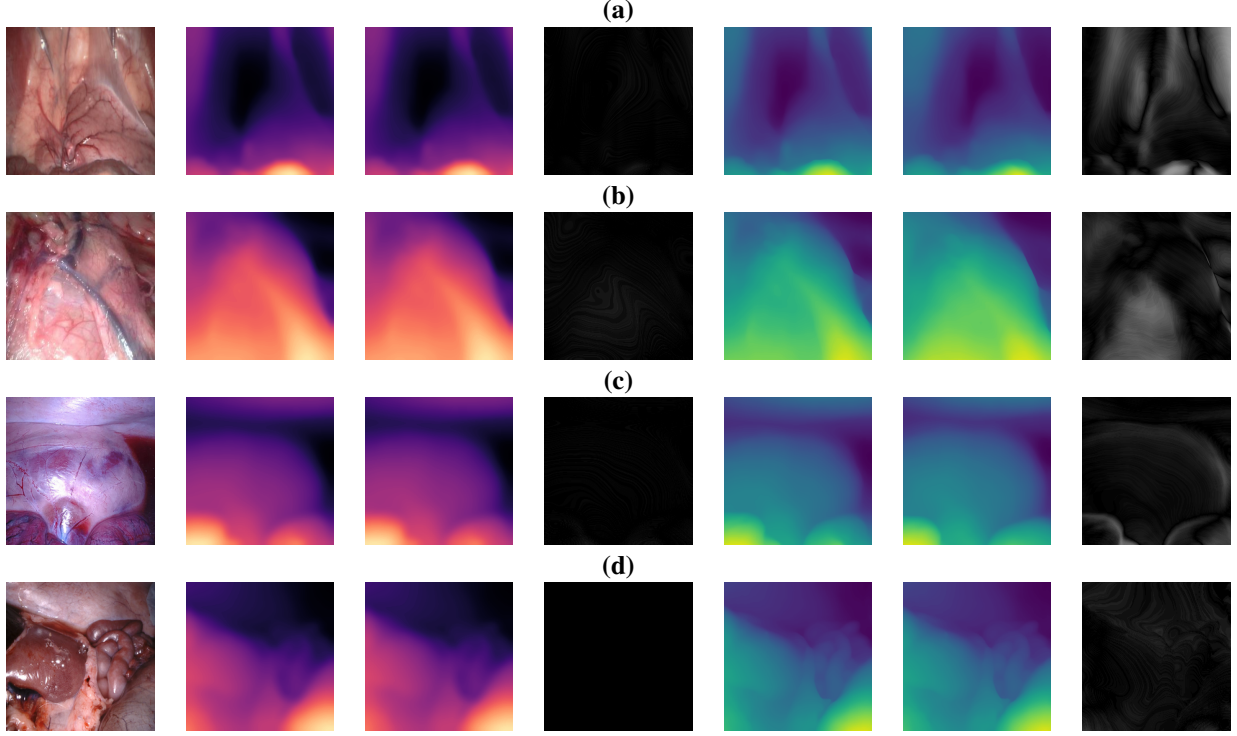


Figure 4: Temporal consistency evaluation across Various HEVD and SCARED datasets [26, 16]. Representative images from the datasets (first column), MAPIS-Depth maps for two consecutive frames (second and third columns) and their pixel-wise differences (fourth column), MDEs [18] (fifth and sixth columns) and their pixel-wise differences (seventh column).

approach in handling complex surgical motion and non-rigid deformations, which are critical for reliable endoscope tracking in MMIS procedures.

To further substantiate the pose estimation capabilities of the proposed framework, the experiment is extended to a broader comparative evaluation against additional existing methods [87, 88, 89, 90, 26], with results summarised in Table 2. The consistent performance across multiple metrics and baselines affirms its applicability for monocular endoscope tracking in dynamic surgical environments.

Table 1: Comprehensive pose error metrics reported as mean \pm standard deviation. All metrics: lower is better (\downarrow). Translation errors are in mm; rotation errors are in degrees ($^\circ$).

Dataset	Framework	Per-axis Errors		Global Errors			Frame-level Errors		
		T_{avg} (mm) \downarrow	R_{avg} ($^\circ$) \downarrow	RMSE (mm) \downarrow	T_{fin} (mm) \downarrow	R_{fin} ($^\circ$) \downarrow	RPE (mm) \downarrow	T_{max} (mm) \downarrow	R_{max} ($^\circ$) \downarrow
S1	Proposed	5.556 ± 3.360	0.061 ± 0.031	6.493	12.224	0.111	6.220 ± 3.533	12.236	0.111
	Endo-2DTAM[84]	12.095 ± 5.782	0.308 ± 0.152	13.406	26.209	0.573	11.614 ± 5.878	26.209	0.573
	OneSLAM [85]	24.555 ± 10.315	0.353 ± 0.174	26.634	40.760	0.470	18.451 ± 10.005	40.760	0.559
	BodySLAM [86]	19.147 ± 8.882	0.536 ± 0.304	21.106	28.440	0.977	16.352 ± 8.359	28.440	0.977
	Endo-Depth-and-Motion [26]	9.966 ± 4.534	0.066 ± 0.032	10.949	16.345	0.106	8.322 ± 4.497	16.351	0.107
S2	Proposed	10.458 ± 3.028	0.188 ± 0.083	10.888	11.188	0.093	10.108 ± 3.191	18.627	0.463
	Endo-2DTAM[84]	19.652 ± 8.199	0.880 ± 0.570	21.293	18.210	1.432	12.498 ± 4.115	28.388	3.105
	OneSLAM [85]	40.286 ± 14.969	0.872 ± 0.379	42.977	32.050	1.057	26.234 ± 9.530	76.255	1.932
	BodySLAM [86]	103.702 ± 48.870	1.650 ± 0.810	114.640	185.537	3.054	96.247 ± 50.492	185.537	3.054
	Endo-Depth-and-Motion [26]	18.754 ± 4.629	0.192 ± 0.050	19.317	17.420	0.194	10.651 ± 2.518	25.694	0.296
S3	Proposed	23.604 ± 12.455	0.304 ± 0.147	26.688	40.247	0.321	31.861 ± 10.880	47.299	0.530
	Endo-2DTAM[84]	38.339 ± 20.230	1.585 ± 1.025	43.350	74.719	2.040	39.045 ± 19.130	75.655	3.138
	OneSLAM [85]	52.214 ± 32.595	0.901 ± 0.451	61.553	49.796	0.978	63.875 ± 22.562	110.902	1.901
	BodySLAM [86]	142.554 ± 92.667	1.332 ± 0.465	170.026	284.527	2.126	190.421 ± 95.401	284.527	2.126
	Endo-Depth-and-Motion [26]	42.898 ± 22.935	0.189 ± 0.087	48.644	70.375	0.366	55.636 ± 24.131	70.464	0.368
S4	Proposed	19.304 ± 11.368	0.061 ± 0.031	22.402	42.783	0.482	24.731 ± 9.424	44.757	0.670
	Endo-2DTAM[84]	21.187 ± 9.214	0.931 ± 0.8311	23.104	29.423	1.229	18.888 ± 7.646	29.806	3.129
	OneSLAM [85]	30.664 ± 18.135	0.259 ± 0.139	35.625	53.065	0.479	30.892 ± 15.196	53.065	0.479
	BodySLAM [86]	85.127 ± 43.828	1.866 ± 0.861	95.747	147.418	2.355	91.727 ± 33.255	148.072	3.142
	Endo-Depth-and-Motion [26]	34.475 ± 22.319	0.423 ± 0.259	41.069	72.736	0.781	40.998 ± 16.859	80.743	0.820

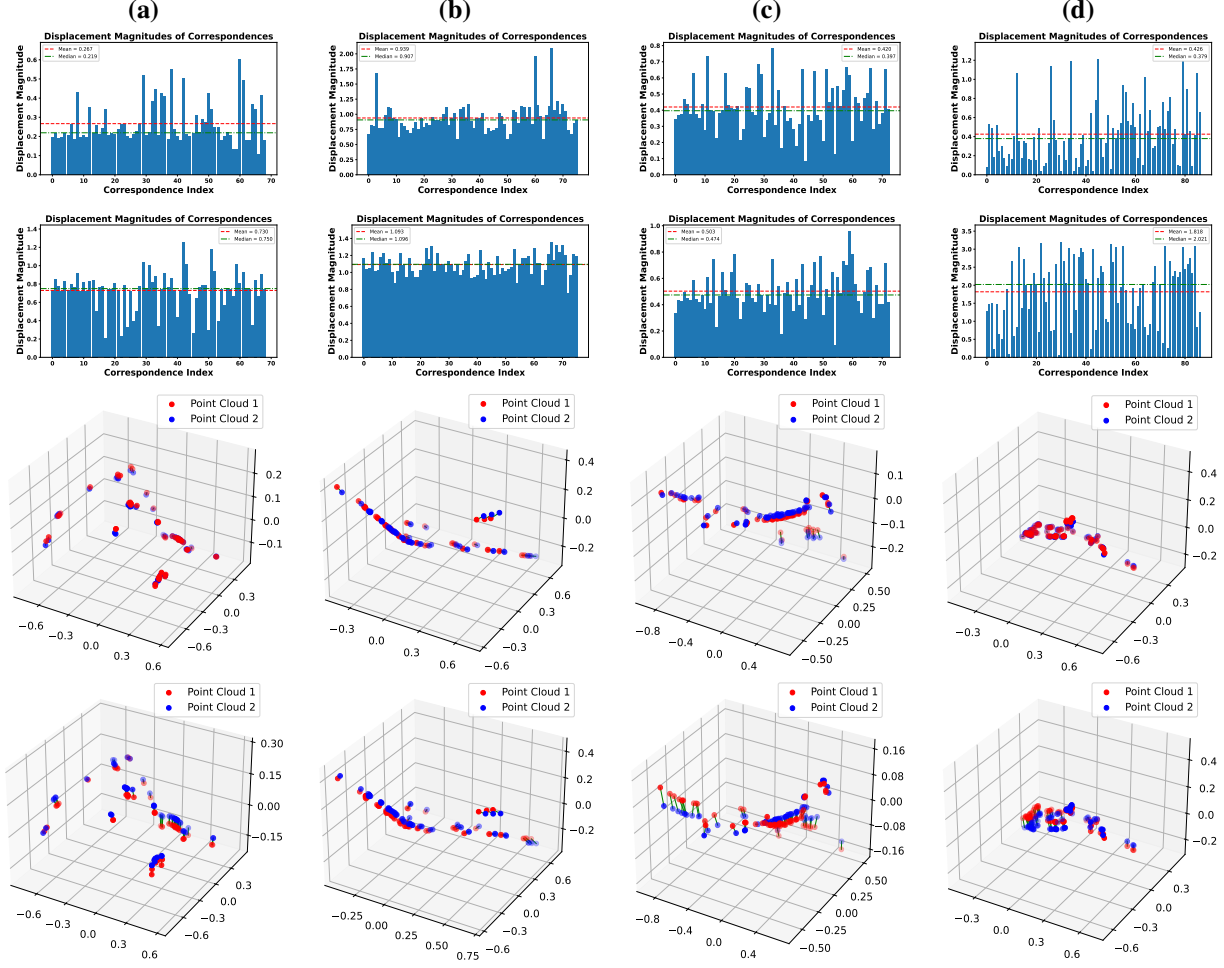


Figure 5: Point-to-point correspondence analysis across datasets (a)-(d), matching the scenes in Fig. 4. First and second rows: displacement magnitudes between matched 3D points derived from MAPIS-Depth and MDEs [18], respectively. Third and fourth rows: corresponding 3D scatter plots of matched point pairs.

Building upon the previous experiments focused on depth consistency and estimated pose accuracy, the fourth experiment demonstrates the framework’s capability to generate accurate 3D reconstructions of tissue surfaces in monocular settings. As illustrated in Fig. 6, the method achieves high-fidelity reconstructions while simultaneously estimating the endoscope trajectory across diverse surgical scenes. Despite challenges such as specular reflections, low tissue contrast, steep surface gradients, abrupt motion, and complex anatomical variations, the framework maintains robust spatial and visual consistency. The overlaid estimated (green) and ground truth (red) trajectories further visualise the accuracy of alignment across the reconstructed surfaces.

To highlight texture preservation, Fig. 7 presents a localised region of a visually complex surface. Panel (a) shows a low-contrast, anatomically irregular area, while panel (b) provides a magnified view of the selected region. The preserved fine-grained textures confirm the framework’s robustness in retaining surface detail and structural coherence, reinforcing its suitability for monocular 3D reconstruction in endoscopic imaging.

The fifth experiment, shown in Table 3, investigates the influence of key architectural components on scale-awareness through an ablation study using the TLR metric. The proposed framework maintains a TLR of 1.000 in *S5*, reflecting ideal scale preservation. However, removing Depth Pro and introducing arbitrary scaling factor values, 30, 100, and 1000, results in considerable TLR deviations from overestimation 1.757 to severe underestimation 0.052, underscoring Depth Pro’s essential role in maintaining scale consistency. Similarly, excluding the optical flow module or temporal smoothing components leads to moderate but consistent TLR degradation, confirming their complementary importance. These trends persist across both the SCARED datasets. This study highlights the TLR as a sensitive and interpretable

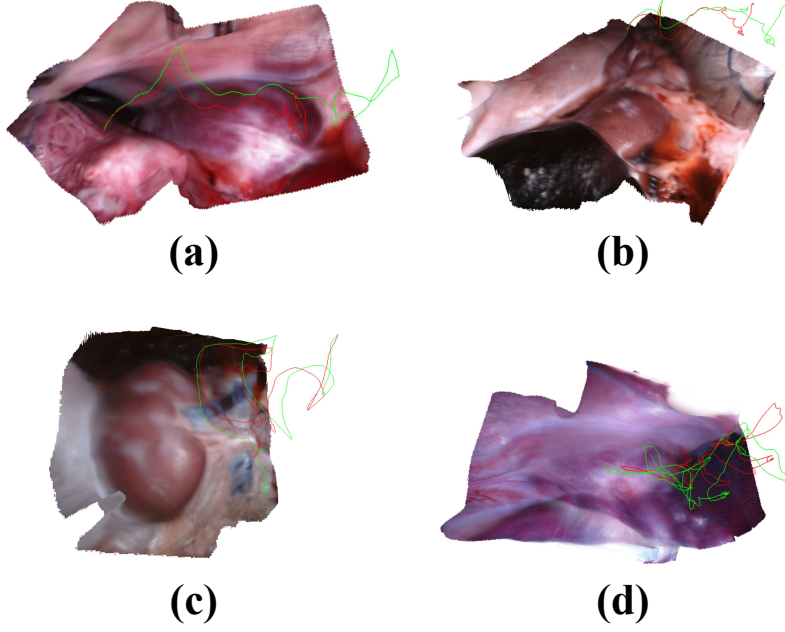


Figure 6: Tissue surface 3D reconstructions with their corresponding estimated (green) and GT (red) trajectories for SCARED datasets [16].

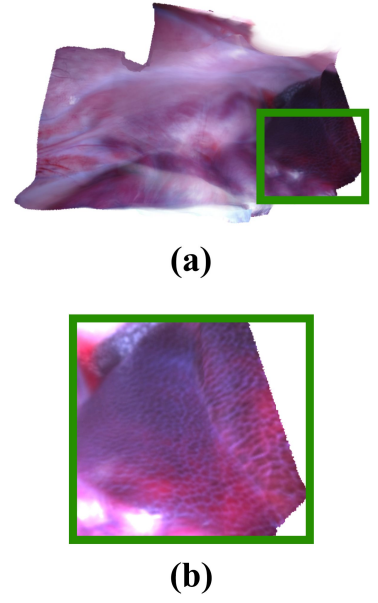


Figure 7: A reconstructed tissue surface with a green rectangle (left) and the rectangle contained region (right) for a SCARED dataset [16].

Table 2: Quantitative comparison between the proposed framework and existing methods [26, 87, 88, 89, 90] on the SCARED dataset in terms of pose estimation accuracy.

Framework	Per-axis Errors		Global Errors		Frame-level Errors			Proportions	
	T_{avg} (mm) ↓	R_{avg} (°) ↓	T_{fn} (mm) ↓	R_{fn} (°) ↓	RPE (mm) ↓	T_{max} (mm) ↓	R_{max} (°) ↓	$T < T_{avg}$ ↑	$R < R_{avg}$ ↑
Proposed	12.551	0.177	15.973	0.342	7.197	18.538	0.347	53.66	50.31
EDAM [26]	17.320	0.171	22.297	0.300	12.845	26.425	0.281	48.43	46.22
Park [90]	17.074	0.206	21.250	0.264	9.713	23.749	0.333	43.73	47.19
SB [89]	16.823	0.197	21.835	0.401	9.962	23.574	0.329	46.76	51.20
Po2Pl [88]	19.015	1.958	20.644	2.648	15.423	31.096	3.135	45.12	41.05
Po2Po [87]	18.554	1.488	19.314	1.322	15.021	31.140	2.367	46.83	47.50

indicator of scale reliability in monocular 3D reconstruction and validates the necessity of each module for preserving scale consistency in dynamic surgical scenes.

The final experiment, shown in Fig. 8, compares the convergence stability of the proposed framework with existing methods [87, 88, 89, 90, 26] using the HEVD dataset [26]. Convergence is assessed based on the number of frames processed before tracking failure occurs. The proposed framework consistently maintains trajectory estimation across the full length of each sequence, reaching the maximum number of frames without failure. In contrast, competing approaches frequently terminate prematurely. These results highlight the framework’s robustness in maintaining long-term stability and resilience under challenging monocular conditions.

5 Conclusion

This work presents a unified framework for monocular endoscope pose estimation and tissue surface reconstruction that addresses depth ambiguity, physiological tissue deformation, inconsistent endoscope motion, limited texture fidelity, and a restricted field of view. The integration of MAPIS-Depth, leveraging Depth Pro for initialisation and Depth Anything for per-frame prediction provides scale-consistent depth estimates. These are temporally refined through RAFT-based correspondence and LPIPS-guided perceptual similarity, mitigating artefacts due to motion and deformation. The WEMA-RTDL module ensures robust pose estimation, and TSDF-based volumetric fusion with marching cubes yields coherent 3D surface meshes. Extensive experimental validation across multiple endoscopic

Table 3: Ablation study corresponding to SCARED datasets [16]. The prefix ‘—’ denotes removal of the specified component from the proposed framework, and the scaling factor indicates replacement of Depth Pro initialisation with a fixed multiplier.

Dataset	Framework	TLR	Per-axis Errors		Global Errors		Frame-level Errors	
			T_{avg} (mm) ↓	R_{avg} (°) ↓	T_{fin} (mm) ↓	R_{fin} (°) ↓	T_{max} (mm) ↓	R_{max} (°) ↓
S5	Proposed	1.000	23.476 ± 1.409	0.063 ± 0.036	23.321	0.138	26.132	0.138
	- Optical Flow	1.343	24.574 ± 0.913	0.062 ± 0.029	26.281	0.109	26.281	0.109
	-Depth Pro (scaling factor=30)	1.757	24.005 ± 1.146	0.057 ± 0.024	26.045	0.111	26.045	0.111
	-Depth Pro (scaling factor=100)	0.520	23.994 ± 1.157	0.058 ± 0.025	26.072	0.113	26.072	0.113
	-Depth Pro (scaling factor=1000)	0.052	23.908 ± 1.180	0.054 ± 0.022	25.869	0.105	25.979	0.105
	- EMA	1.088	23.969 ± 1.138	0.063 ± 0.035	24.780	0.137	26.140	0.137
	- DyEMA	1.247	24.590 ± 0.992	0.063 ± 0.032	26.855	0.129	26.855	0.129
S6	Proposed	0.824	8.111 ± 3.621	0.457 ± 0.175	11.519	0.849	16.932	0.219
	- Optical Flow	1.164	12.890 ± 5.637	0.411 ± 0.177	22.786	0.706	22.786	0.299
	-Depth Pro (scaling factor=30)	0.990	10.102 ± 4.172	0.517 ± 0.209	18.028	0.902	20.092	0.344
	-Depth Pro (scaling factor=100)	0.297	9.787 ± 4.176	0.506 ± 0.204	17.380	0.897	19.537	0.344
	-Depth Pro (scaling factor=1000)	0.030	9.857 ± 4.252	0.507 ± 0.206	17.578	0.905	19.712	0.344
	- EMA	0.700	7.753 ± 3.670	0.467 ± 0.177	8.482	0.847	16.970	0.344
	- DyEMA	0.818	8.116 ± 3.741	0.467 ± 0.175	11.082	0.847	17.583	0.344

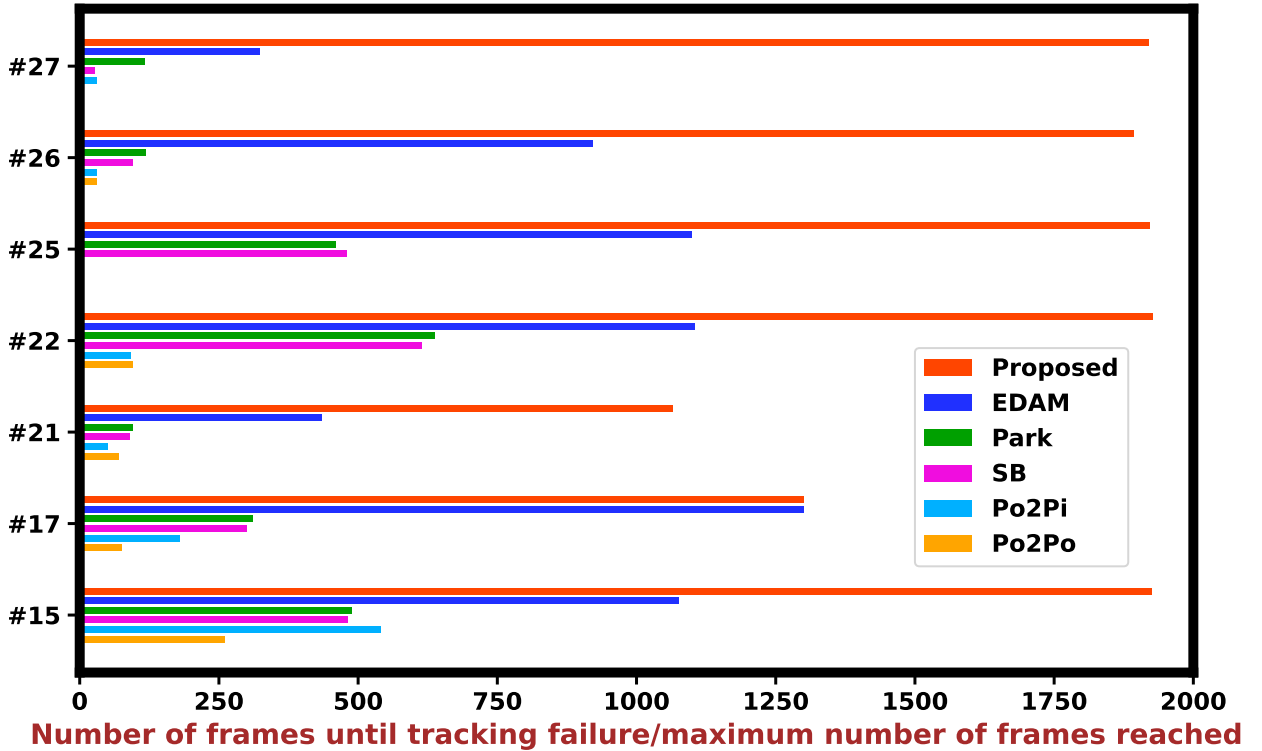


Figure 8: Result comparison between the proposed and existing frameworks [87, 88, 89, 90, 26] in terms of tracking convergence failures on various HEVD datasets [26] as shown along the vertical axis.

datasets confirms the framework’s superiority in tissue reconstruction, demonstrating improved depth consistency, precise endoscope pose estimation, and enhanced scale awareness compared to existing approaches. Future work may explore uncertainty-guided refinement and multimodal integration, extending its applicability to real-time robotic surgery and intraoperative decision support.

References

- [1] Desmond H Birkett. Three-dimensional laparoscopy. *Journal of laparoendoscopic surgery*, 5(5):327–331, 1995.
- [2] Toby Collins and Adrien Bartoli. Towards live monocular 3d laparoscopy using shading and specular information. In *International Conference on Information Processing in Computer-Assisted Interventions*, pages 11–21, 2012.
- [3] Antony J Hodgson, John G Person, Septimiu E Salcudean, and Alex G Nagy. The effects of physical constraints in laparoscopic surgery. *Medical Image Analysis*, 3(3):275–283, 1999.
- [4] Christopher Limb and Timothy Rockall. Principles of laparoscopic surgery. *Surgery (Oxford)*, 41(2):106–116, 2023.
- [5] Ziteng Liu, Wenpeng Gao, Jiahua Zhu, Zhi Yu, and Yili Fu. Surface deformation tracking in monocular laparoscopic video. *Medical image analysis*, 86:102775, 2023.
- [6] Enpeng Wang, Yueang Liu, Jiangchang Xu, and Xiaojun Chen. Non-rigid scene reconstruction of deformable soft tissue with monocular endoscopy in minimally invasive surgery. *International Journal of Computer Assisted Radiology and Surgery*, pages 1–11, 2024.
- [7] Michel Hayoz, Christopher Hahne, Mathias Gallardo, Daniel Candinas, Thomas Kurmann, Maximilian Allan, and Raphael Sznitman. Learning how to robustly estimate camera pose in endoscopic videos. *International Journal of Computer Assisted Radiology and Surgery*, 18(7):1185–1192, 2023.
- [8] Haibin Wu, Ruotong Xu, Kaiyang Xu, Jianbo Zhao, Yan Zhang, Aili Wang, and Yuji Iwahori. 3d texture reconstruction of abdominal cavity based on monocular vision slam for minimally invasive surgery. *Symmetry*, 14(2):185, 2022.
- [9] A Verri and V Torre. Absolute depth estimate in stereopsis. *JOSA A*, 3(3):297–299, 1986.
- [10] Feng Shao, Weisi Lin, Gangyi Jiang, and Qionghai Dai. Models of monocular and binocular visual perception in quality assessment of stereoscopic images. *IEEE Transactions on Computational Imaging*, 2(2):123–135, 2016.
- [11] Vasileios Arampatzakis, George Pavlidis, Nikolaos Mitianoudis, and Nikos Papamarkos. Monocular depth estimation: A thorough review. *IEEE Transactions on Pattern Analysis and Machine Intelligence*, 2023.
- [12] Yongzhi Su, Yan Di, Guangyao Zhai, Fabian Manhardt, Jason Rambach, Benjamin Busam, Didier Stricker, and Federico Tombari. Opa-3d: Occlusion-aware pixel-wise aggregation for monocular 3d object detection. *IEEE Robotics and Automation Letters*, 8(3):1327–1334, 2023.
- [13] Sang-Ah Yoo, Suhyun Lee, and Sung Jun Joo. Monocular cues are superior to binocular cues for size perception when they are in conflict in virtual reality. *Cortex*, 166:80–90, 2023.
- [14] Paul B Hibbard, Ross Goutcher, Rebecca L Hornsey, David W Hunter, and Peter Scarfe. Luminance contrast provides metric depth information. *Royal Society Open Science*, 10(2):220567, 2023.
- [15] Yifan Wang, Liang Zhao, Lun Gong, Xin Chen, and Siyang Zuo. A monocular slam system based on sift features for gastroscope tracking. *Medical & Biological Engineering & Computing*, 61(2):511–523, 2023.
- [16] Max Allan, Jonathan Mcleod, Congcong Wang, Jean Claude Rosenthal, Zhenglei Hu, Niklas Gard, Peter Eisert, Ke Xue Fu, Trevor Zeffiro, Wenya Xia, et al. Stereo correspondence and reconstruction of endoscopic data challenge. *arXiv preprint arXiv:2101.01133*, 2021.
- [17] Taylor L Bobrow, Mayank Golhar, Rohan Vijayan, Venkata S Akshintala, Juan R Garcia, and Nicholas J Durr. Colonoscopy 3d video dataset with paired depth from 2d-3d registration. *Medical image analysis*, 90:102956, 2023.
- [18] Aleksei Bochkovskii, Amaël Delaunoy, Hugo Germain, Marcel Santos, Yichao Zhou, Stephan R Richter, and Vladlen Koltun. Depth pro: Sharp monocular metric depth in less than a second. *arXiv preprint arXiv:2410.02073*, 2024.
- [19] Lihe Yang, Bingyi Kang, Zilong Huang, Xiaogang Xu, Jiashi Feng, and Hengshuang Zhao. Depth anything: Unleashing the power of large-scale unlabeled data. In *International Conference on Computer Vision and Pattern Recognition*, pages 10371–10381, 2024.

- [20] Zachary Teed and Jia Deng. Raft: Recurrent all-pairs field transforms for optical flow. In *European Conference on Computer Vision*, pages 402–419, 2020.
- [21] Richard Zhang, Phillip Isola, Alexei A Efros, Eli Shechtman, and Oliver Wang. The unreasonable effectiveness of deep features as a perceptual metric. In *International Conference on Computer Vision and Pattern Recognition*, pages 586–595, 2018.
- [22] Boris Makaeu and Ilya Afanasyev. The software tool for comparison and configuration of nonlinear optimization techniques in orb-slam. In *International Conference on Developments in eSystems Engineering*, pages 489–494, 2019.
- [23] Robert G Brown. *Exponential smoothing for predicting demand*. Little, 1956.
- [24] Brian Curless and Marc Levoy. A volumetric method for building complex models from range images. In *Annual Conference on Computer Graphics and Interactive Techniques*, pages 303–312, 1996.
- [25] William E Lorensen and Harvey E Cline. Marching cubes: A high resolution 3d surface construction algorithm. In *Seminal graphics: pioneering efforts that shaped the field*, pages 347–353. 1998.
- [26] David Recasens, José Lamarca, José M Fácil, JMM Montiel, and Javier Civera. Endo-depth-and-motion: Reconstruction and tracking in endoscopic videos using depth networks and photometric constraints. *IEEE Robotics and Automation Letters*, 6(4):7225–7232, 2021.
- [27] Taha Samavati and Mohsen Soryani. Deep learning-based 3d reconstruction: a survey. *Artificial Intelligence Review*, 56(9):9175–9219, 2023.
- [28] Anis Farshian, Markus Götz, Gabriele Cavallaro, Charlotte Debus, Matthias Nießner, Jón Atli Benediktsson, and Achim Streit. Deep-learning-based 3-d surface reconstruction—a survey. *Proceedings of the IEEE*, 2023.
- [29] Riku Murai, Eric Dexheimer, and Andrew J Davison. Mast3r-slam: Real-time dense slam with 3d reconstruction priors. *arXiv preprint arXiv:2412.12392*, 2024.
- [30] Hidenobu Matsuki, Riku Murai, Paul HJ Kelly, and Andrew J Davison. Gaussian splatting slam. In *International Conference on Computer Vision and Pattern Recognition*, pages 18039–18048, 2024.
- [31] Zhiwen Fan, Kairun Wen, Wenyan Cong, Kevin Wang, Jian Zhang, Xinghao Ding, Danfei Xu, Boris Ivanovic, Marco Pavone, Georgios Pavlakos, et al. Instantsplat: Sparse-view sfm-free gaussian splatting in seconds. *arXiv preprint arXiv:2403.20309*, 2024.
- [32] Hans Peter Moravec. *Obstacle avoidance and navigation in the real world by a seeing robot rover*. Stanford University, 1980.
- [33] João Carlos Virgolino Soares, Marcelo Gattass, and Marco Antonio Meggiolaro. Crowd-slam: visual slam towards crowded environments using object detection. *Journal of Intelligent & Robotic Systems*, 102(2):50, 2021.
- [34] Shih Wen Hsiao and Rong Qi Chen. A study of surface reconstruction for 3d mannequins based on feature curves. *Computer-Aided Design*, 45(11):1426–1441, 2013.
- [35] Volker Blanz, Albert Mehler, Thomas Vetter, and H P Seidel. A statistical method for robust 3d surface reconstruction from sparse data. In *International Symposium on 3D Data Processing, Visualization and Transmission*, pages 293–300, 2004.
- [36] Maxime Lhuillier and Long Quan. A quasi-dense approach to surface reconstruction from uncalibrated images. *IEEE Transactions on Pattern Analysis and Machine Intelligence*, 27(3):418–433, 2005.
- [37] Elisa Dall’Asta and Riccardo Roncella. A comparison of semiglobal and local dense matching algorithms for surface reconstruction. *The International Archives of the Photogrammetry, Remote Sensing and Spatial Information Sciences*, 40:187–194, 2014.
- [38] Hyungjun Park. A hybrid approach to smooth surface reconstruction from 2-d cross sections. *The International Journal of Advanced Manufacturing Technology*, 25:1130–1136, 2005.
- [39] Takafumi Taketomi, Hideaki Uchiyama, and Sei Ikeda. Visual slam algorithms: A survey from 2010 to 2016. *IPSJ Transactions on Computer Vision and Applications*, 9:1–11, 2017.
- [40] Woo Yeon Jeong and Kyoung Mu Lee. Visual slam with line and corner features. In *International Conference on Intelligent Robots and Systems*, pages 2570–2575. IEEE, 2006.
- [41] Raul Mur-Artal, Jose Maria Martinez Montiel, and Juan D Tardos. Orb-slam: a versatile and accurate monocular slam system. *IEEE Transactions on Robotics*, 31(5):1147–1163, 2015.
- [42] Carlos Campos, Richard Elvira, Juan J Gómez Rodríguez, José MM Montiel, and Juan D Tardós. Orb-slam3: An accurate open-source library for visual, visual-inertial, and multimap slam. *IEEE Transactions on Robotics*, 37(6):1874–1890, 2021.

- [43] Robert Castle. Parallel tracking and multiple mapping (ptamm) manual. *Robotics Research Group, Department of Engineering Science, University of Oxford*, 2010.
- [44] David G Lowe. Object recognition from local scale-invariant features. In *International Conference on Computer Vision*, volume 2, pages 1150–1157, 1999.
- [45] Herbert Bay, Andreas Ess, Tinne Tuytelaars, and Luc Van Gool. Speeded-up robust features (surf). *Computer Vision and Image Understanding*, 110(3):346–359, 2008.
- [46] Ethan Rublee, Vincent Rabaud, Kurt Konolige, and Gary Bradski. Orb: An efficient alternative to sift or surf. In *International Conference on Computer Vision*, pages 2564–2571, 2011.
- [47] Martin A Fischler and Robert C Bolles. Random sample consensus: A paradigm for model fitting with applications to image analysis and automated cartography. *Communications of the ACM*, 24(6):381–395, 1981.
- [48] Bill Triggs, Philip F McLauchlan, Richard I Hartley, and Andrew W Fitzgibbon. Bundle adjustment—a modern synthesis. In *Vision Algorithms: Theory and Practice*, pages 298–372, 2000.
- [49] Oscar G Grasa, Javier Civera, and JMM Montiel. Ekf monocular slam with relocalization for laparoscopic sequences. In *International Conference on Robotics and Automation*, pages 4816–4821, 2011.
- [50] Ruben Martinez Cantin and José A Castellanos. Unscented slam for large-scale outdoor environments. In *International Conference on Intelligent Robots and Systems*, pages 3427–3432, 2005.
- [51] Steven Holmes, Georg Klein, and David W Murray. A square root unscented kalman filter for visual monoslam. In *International Conference on Robotics and Automation*, pages 3710–3716, 2008.
- [52] Zhang Yanhao, Cheng Chonghao, Falque Raphael, Zhao Liang, Huang Shoudong, and Chen Yongbo. 3d intra-articular dense reconstruction from arthroscopic images. In *International Conference on Robotics and Biomimetics*, pages 1–7, 2023.
- [53] Yang Li, Florian Richter, Jingpei Lu, Emily K Funk, Ryan K Orosco, Jianke Zhu, and Michael C Yip. Super: A surgical perception framework for endoscopic tissue manipulation with surgical robotics. *IEEE Robotics and Automation Letters*, 5(2):2294–2301, 2020.
- [54] Nader Mahmoud, Toby Collins, Alexandre Hostettler, Luc Soler, Christophe Doignon, and Jose Maria Martinez Montiel. Live tracking and dense reconstruction for handheld monocular endoscopy. *IEEE Transactions on Medical Imaging*, 38(1):79–89, 2018.
- [55] Shuai Wang, Zhizhe Yu, Yudi Zhao, and Yunpeng Zhu. Advanced algorithms of slam in medical endoscopy. In *AIP Conference Proceedings*, volume 3017, 2023.
- [56] Junjie Zhao, Yang Luo, Qimin Li, Natalie Baddour, and Md Sulayman Hossen. Spsvo: A self-supervised surgical perception stereo visual odometer for endoscopy. *Robotica*, 41(12):3724–3745, 2023.
- [57] Tinghui Zhou, Matthew Brown, Noah Snavely, and David G Lowe. Unsupervised learning of depth and ego-motion from video. In *International Conference on Computer Vision and Pattern Recognition*, pages 1851–1858, 2017.
- [58] Ruihao Li, Sen Wang, and Dongbing Gu. Ongoing evolution of visual slam from geometry to deep learning: Challenges and opportunities. *Cognitive Computation*, 10(6):875–889, 2018.
- [59] Ruihao Li, Qiang Liu, Jianjun Gui, Dongbing Gu, and Huosheng Hu. Indoor relocalization in challenging environments with dual-stream convolutional neural networks. *IEEE Transactions on Automation Science and Engineering*, 15(2):651–662, 2017.
- [60] Ronald Clark, Sen Wang, Andrew Markham, Niki Trigoni, and Hongkai Wen. Vidloc: A deep spatio-temporal model for 6-dof video-clip relocalization. In *International Conference on Computer Vision and Pattern Recognition*, pages 6856–6864, 2017.
- [61] Alex Kendall, Matthew Grimes, and Roberto Cipolla. Posenet: A convolutional network for real-time 6-dof camera relocalization. In *International Conference on Computer Vision*, pages 2938–2946, 2015.
- [62] Sen Wang, Ronald Clark, Hongkai Wen, and Niki Trigoni. Deepvo: Towards end-to-end visual odometry with deep recurrent convolutional neural networks. In *International Conference on Robotics and Automation*, pages 2043–2050, 2017.
- [63] Ruihao Li, Sen Wang, Zhiqiang Long, and Dongbing Gu. Undeepvo: Monocular visual odometry through unsupervised deep learning. In *International Conference on Robotics and Automation*, pages 7286–7291, 2018.
- [64] Zihan Zhu, Songyou Peng, Viktor Larsson, Weiwei Xu, Hujun Bao, Zhaopeng Cui, Martin R Oswald, and Marc Pollefeys. Nice-slam: Neural implicit scalable encoding for slam. In *International Conference on Computer Vision and Pattern Recognition*, pages 12786–12796, 2022.

- [65] Clement Godard, Oisin Mac Aodha, and Gabriel J Brostow. Unsupervised monocular depth estimation with left-right consistency. In *International Conference on Computer Vision*, pages 270–279, 2017.
- [66] Daniel A Hashimoto, Guy Rosman, Daniela Rus, and Ozanan R Meireles. Artificial intelligence in surgery: Promises and perils. *Annals of surgery*, 268(1):70–76, 2018.
- [67] Kailing Wang, Chen Yang, Yuehao Wang, Sikuang Li, Yan Wang, Qi Dou, Xiaokang Yang, and Wei Shen. Endogslam: Real-time dense reconstruction and tracking in endoscopic surgeries using gaussian splatting. *arXiv preprint arXiv:2403.15124*, 2024.
- [68] Bernhard Kerbl, Georgios Kopanas, Thomas Leimkühler, and George Drettakis. 3d gaussian splatting for real-time radiance field rendering. *ACM Trans. Graph.*, 42(4):139–1, 2023.
- [69] G Manni, C Lauretti, F Prata, R Papalia, L Zollo, and P Soda. Bodyslam: A generalized monocular visual slam framework for surgical applications. *arXiv preprint arXiv:2408.03078*, 2024.
- [70] Shariq Farooq Bhat, Reiner Birkel, Diana Wofk, Peter Wonka, and Matthias Müller. Zoedepth: Zero-shot transfer by combining relative and metric depth. *arXiv preprint arXiv:2302.12288*, 2023.
- [71] Liang Li, Sophia Bano, Jan Deprest, Anna L David, Danail Stoyanov, and Francisco Vasconcelos. Globally optimal fetoscopic mosaicking based on pose graph optimisation with affine constraints. *IEEE Robotics and Automation Letters*, 6(4):7831–7838, 2021.
- [72] Kai Han, Yunhe Wang, Hanqing Chen, Xinghao Chen, Jianyuan Guo, Zhenhua Liu, Yehui Tang, An Xiao, Chunjing Xu, Yixing Xu, et al. A survey on vision transformer. *IEEE Transactions on Pattern Analysis and Machine Intelligence*, 45(1):87–110, 2022.
- [73] Ciyu Zhu, Richard H Byrd, Peihuang Lu, and Jorge Nocedal. Algorithm 778: L-bfgs-b: Fortran subroutines for large-scale bound-constrained optimization. *ACM Transactions on Mathematical Software*, 23(4):550–560, 1997.
- [74] G. Bradski. The OpenCV Library. *Dr. Dobb’s Journal of Software Tools*, 2000.
- [75] Carlo Tomasi and Roberto Manduchi. Bilateral filtering for gray and color images. In *International Conference on Computer Vision*, pages 839–846, 1998.
- [76] Alex Krizhevsky, Ilya Sutskever, and Geoffrey E Hinton. Imagenet classification with deep convolutional neural networks. *Communications of the ACM*, 60(6):84–90, 2017.
- [77] Richard Hartley and Andrew Zisserman. *Multiple view geometry in computer vision*. Cambridge University Press, 2003.
- [78] Carl Friedrich Gauss. *Theoria motus corporum coelestium in sectionibus conicis solem ambientium auctore Carolo Friderico Gauss*. sumtibus Frid. Perthes et IH Besser, 1809.
- [79] Haskell B Curry. The method of steepest descent for non-linear minimization problems. *Quarterly of Applied Mathematics*, 2(3):258–261, 1944.
- [80] Samunda Perera, Nick Barnes, Xuming He, Shahram Izadi, Pushmeet Kohli, and Ben Glocker. Motion segmentation of truncated signed distance function based volumetric surfaces. In *Winter Conference on Applications of Computer Vision*, pages 1046–1053, 2015.
- [81] Jürgen Sturm, Nikolas Engelhard, Felix Endres, Wolfram Burgard, and Daniel Cremers. A benchmark for the evaluation of rgb-d slam systems. In *International Conference on Intelligent Robots and Systems*, pages 573–580, 2012.
- [82] Matteo Luperto, Valerio Castelli, and Francesco Amigoni. Predicting performance of slam algorithms. *arXiv preprint arXiv:2109.02329*, 2021.
- [83] Marco Wagner and Devesh Vashisth. The influence of inaccurate gpu power measurements for machine learning workloads in industrial applications. In *International Conference on Human-Computer Interaction*, pages 233–247. Springer, 2025.
- [84] Yiming Huang, Beilei Cui, Long Bai, Zhen Chen, Jinlin Wu, Zhen Li, Hongbin Liu, and Hongliang Ren. Advancing dense endoscopic reconstruction with gaussian splatting-driven surface normal-aware tracking and mapping. *arXiv preprint arXiv:2501.19319*, 2025.
- [85] Timo Teufel, Hongchao Shu, Roger D Soberanis-Mukul, Jan Emily Mangulabnan, Manish Sahu, S Swaroop Vedula, Masaru Ishii, Gregory Hager, Russell H Taylor, and Mathias Unberath. Oneslam to map them all: A generalized approach to slam for monocular endoscopic imaging based on tracking any point. *International Journal of Computer Assisted Radiology and Surgery*, 19(7):1259–1266, 2024.
- [86] Dorian F Henning, Tristan Laidlow, and Stefan Leutenegger. Bodyslam: Joint camera localisation, mapping, and human motion tracking. In *European Conference on Computer Vision*, pages 656–673. Springer, 2022.

- [87] Paul J Besl and Neil D McKay. Method for registration of 3-d shapes. In *Sensor fusion IV: Control paradigms and data structures*, volume 1611, pages 586–606. Spie, 1992.
- [88] Yang Chen and Gérard Medioni. Object modelling by registration of multiple range images. *Image and Vision Computing*, 10(3):145–155, 1992.
- [89] Frank Steinbrücker, Jürgen Sturm, and Daniel Cremers. Real-time visual odometry from dense rgb-d images. In *International Conference on Computer Vision*, pages 719–722, 2011.
- [90] Jaesik Park, Qian-Yi Zhou, and Vladlen Koltun. Colored point cloud registration revisited. In *International Conference on Computer Vision*, pages 143–152, 2017.